www.sciencemag.org/content/351/6269/151/suppl/DC1

Supplementary Materials for

A mixed-cation lead mixed-halide perovskite absorber for tandem solar cells

David P. McMeekin, Golnaz Sadoughi, Waqaas Rehman, Giles E. Eperon, Michael Saliba, Maximilian T. Hörantner, Amir Haghighirad, Nobuya Sakai, Lars Korte, Bernd Rech, Michael B. Johnston, Laura M. Herz, Henry J. Snaith*

*Corresponding author. E-mail: henry.snaith@physics.ox.ac.uk

Published 8 January 2016, *Science* **351**, 151 (2016)
DOI: 10.1126/science.aad5845

This PDF file includes:

Materials and Methods

Materials

Unless otherwise stated, all materials were purchased from Sigma-Aldrich or Alfa Aesar and used as received. Spiro-OMeTAD was purchased from Borun Chemicals and used as received.

Perovskite precursor synthesis:

Formamidinium iodide (FAI) and formamidinium bromide (FABr) were synthesised by dissolving formamidinium acetate powder in a 1.5x molar excess of 57%w/w hydroiodic acid (HI), or 48% w/w hydrobromic acid (for FABr). After addition of acid the solution was left stirring for 10 minutes at 50°C. Upon drying at 100°C for 2h, a yellow-white powder is formed. This was then washed three times with diethyl ether. The power was later dissolved in ethanol heated at 80°C to obtain a supersaturate solution. Once fully dissolved, the solution is then placed in a refrigerator for overnight recrystallization. The recrystallization process forms white needle-like crystals. The powder is later washed with diethyl ether three times. Finally, the powder is dried overnight in a vacuum oven at 50°C.

Perovskite precursor solution mixture

For XRD and optical measurements, we formed two series of films ranging from neat I to neat Br; one with FA as the only cation and one with 83% FA and 17% Cs. To form each specific composition ranging from neat Br to neat I, two separate precursor solutions were made: $FAPbI_3$ and $FAPbBr_3$, for the FA series. Two additional precursor solutions were made: $FA_{0.83}Cs_{0.17}PbI_3$ and $FA_{0.83}Cs_{0.17}PbBr_3$, for the FA/Cs series. All solutions were dissolved in anhydrous N,N-dimethylformamide (DMF) to obtain a stoichiometric solution with desired composition using precursor salts: FAI, FABr, CsI, CsBr, PbI_2, $PbBr_2$. 31.7µl of 57%w/w hydroiodic acid (HI) and 18.8µl of 48%w/w hydrobromic acid (HBr) was added to 1ml of 0.55M precursor solutions for both solutions. To form the $FA_{0.83}Cs_{0.17}Pb(I_{0.6}Br_{0.4})_3$ "optimized precursor solution composition" used for the device fabrication, FAI, CsI, $PbBr_2$ and PbI_2 were dissolved in DMF to obtain a stoichiometric solution with desired composition and a molar concentration of 0.95M. 54.7µl of HI and 27.3µl of HBr was added to 1ml of 0.95M precursor solutions. After the addition of the acids, the solution was stirred for 72 hours under a nitrogen atmosphere.

Perovskite solar cell fabrication

The precursor perovskite solution was spin-coated in a nitrogen-filled glovebox at 2000rpm for 45s, on a substrate pre-heated at 70°C. The films were dried inside a N_2 glovebox on a hot plate at a temperature of 70°C for 1 minute. The films were then annealed in an oven in an air atmosphere at 185°C for 90 minutes.

Hole-transporting layer fabrication

The electron-blocking layer was deposited with a 96mg/ml of 2,2',7,7'-tetrakis-(N,N-di-p-methoxyphenylamine)9,9'-spirobifluorene (spiro-OMeTAD) solution in

chlorobenzene. Additives of 32μl of lithium bis(trifluoromethanesulfonyl)imide (170mg/ml 1-butanol solution) per 1ml of spiro-OMeTAD solution and 10ul of 4-tert-butylpyridine per 1ml of spiro-OMeTAD solution. Spin-coating was carried out in a nitrogen-filled glovebox at 2000rpm for 60s.

Electrode

A 120nm silver electrode was thermally evaporated under vacuum of $\approx 10^{-6}$ Torr, at a rate of ≈ 0.2 nm$\cdot$s^{-1}.

Device characterization

The current density–voltage (J-V) curves were measured (2400 Series SourceMeter, Keithley Instruments) under simulated AM 1.5 sunlight at 100 mWcm^{-2} irradiance generated by an Abet Class AAB sun 2000 simulator, with the intensity calibrated with an NREL calibrated KG5 filtered Si reference cell. The mismatch factor was calculated to be less than 1%. The active area of the solar cell is 0.0919 cm^{-2}. The forward J–V scans were measured from forward bias (FB) to short circuit (SC) and the backward scans were from short circuit to forward bias, both at a scan rate of 0.38V s^{-1}. A stabilization time of 5s at forward bias of 1.4 V under illumination was done prior to scanning. The EQE was measured using Fourier transform photocurrent spectroscopy. The EQE was measured in short-circuit (Jsc) configuration following a 1.4V prebias for 20s, using a simulated air-mass (AM) 1.5 100 mW cm-2 sun light as illumination source.

Substrate Preparation

Devices were fabricated on fluorine-doped tin oxide (FTO) coated glass (Pilkington, 7Ω □$^{-1}$). Initially, FTO was removed at specific regions where the anode contact will be deposited. This FTO etching was done using a 2M HCl and zinc powder. Substrates were then cleaned sequentially in hallmanex detergent, acetone, isopropyl alcohol. The FTO was then cleaned for 10 minutes using oxygen plasma. A hole-blocking layer was formed by immersing the cleaned FTO substrate in a bath of 40mM $SnCl_4$ in aqueous solution for 30 minutes at 80°C (*38*). The substrates were immediately rinsed with two consecutive deionized water baths and then sonicated for 10s in an ethanol bath. The substrates were then dried with a nitrogen gun. A 7.5mg/ml of Phenyl-C60-butyric acid methyl ester (PCBM) solution in chlorobenzene was then spin coated inside a N_2 glovebox onto the SnO_2 compact layer at 2000 rpm for 45 seconds and annealed at 70°C for 10 minutes (*39*, *40*).

Optical pump - THz probe spectroscopy

The optical-pump-THz-probe setup uses a Spectra Physics Ti:Sapphire regenerative amplifier to generate 40 fs pulses at a center wavelength of 800 nm and a repetition rate of 1.1kHz. Terahertz pulses were generated by optical rectification in a 450 μm thick GaP(110) single crystal and detected by electro-optic sampling in a ZnTe crystal (0.2mm (110)-ZnTe on 3mm (100)-ZnTe). Pulses for optical excitation of the samples at 400nm have been generated using a beta barium borat frequency doubling crystal. Optical excitation was carried out from the substrate side of the film. The diameters of optical pump and THz probe beams at the sample position were 3.6 mm and 2.4 mm (FWHM),

respectively. Measurements were performed with the entire THz beam path (including emitter, detector and sample) in an evacuated chamber at a pressure of $<10^{-2}$ bar.

Solar cell fabrication

The experimental details on the silicon cell fabrication can be found elsewhere (37). Briefly, both-side random pyramid textured float zone n-type <100> oriented wafers with 4 inch diameter, ~250 µm thickness, and a resistivity of 2-5 Ω·cm were used. The wafers were cleaned using the standard RCA process and the resulting oxides were removed by dipping in diluted hydrofluoric acid immediately before a-Si:H deposition. Intrinsic a-Si:H layers were deposited by standard PECVD processes using silane, SiH_4, as precursor gas. The n-type and p-type doped a-Si:H layers were prepared by adding PH3 or B2H6 to the precursor gas, respectively. On the front side of the wafer, 80 nm ITO was deposited by RF magnetron sputter deposition from a ceramic target at room temperature. The back contact was formed by sputtering 80 nm of aluminum doped zinc oxide (AZO) and 200 nm silver in a Leybold Optics A600V7 tool. The front side contact grid consists of a stack of 10 nm Ti and 1500 nm Ag, thermally evaporated through a shadow mask. Following this fabrication process, the cells were annealed at 160°C for 70 min in air.

Transparent electrode

A thin layer of ITO (Indium Tin Oxide) nanoparticles (<100nm), from ITO dispersion in isopropanol, was spin coated on hole transport layer as the buffer layer to protect the spiro-OMeTAD during ITO sputtering. Then a ~120-nm thick layer of ITO was sputter coated on the buffer layer using a PVD 75 Kurt J. Lesker.

Supplementary Text

$FAPb(I_{(1-x)}Br_{(x)})_3$ and $FA_{0.83}Cs_{0.17}Pb(I_{(1-x)}Br_x)_3$ perovskites systems

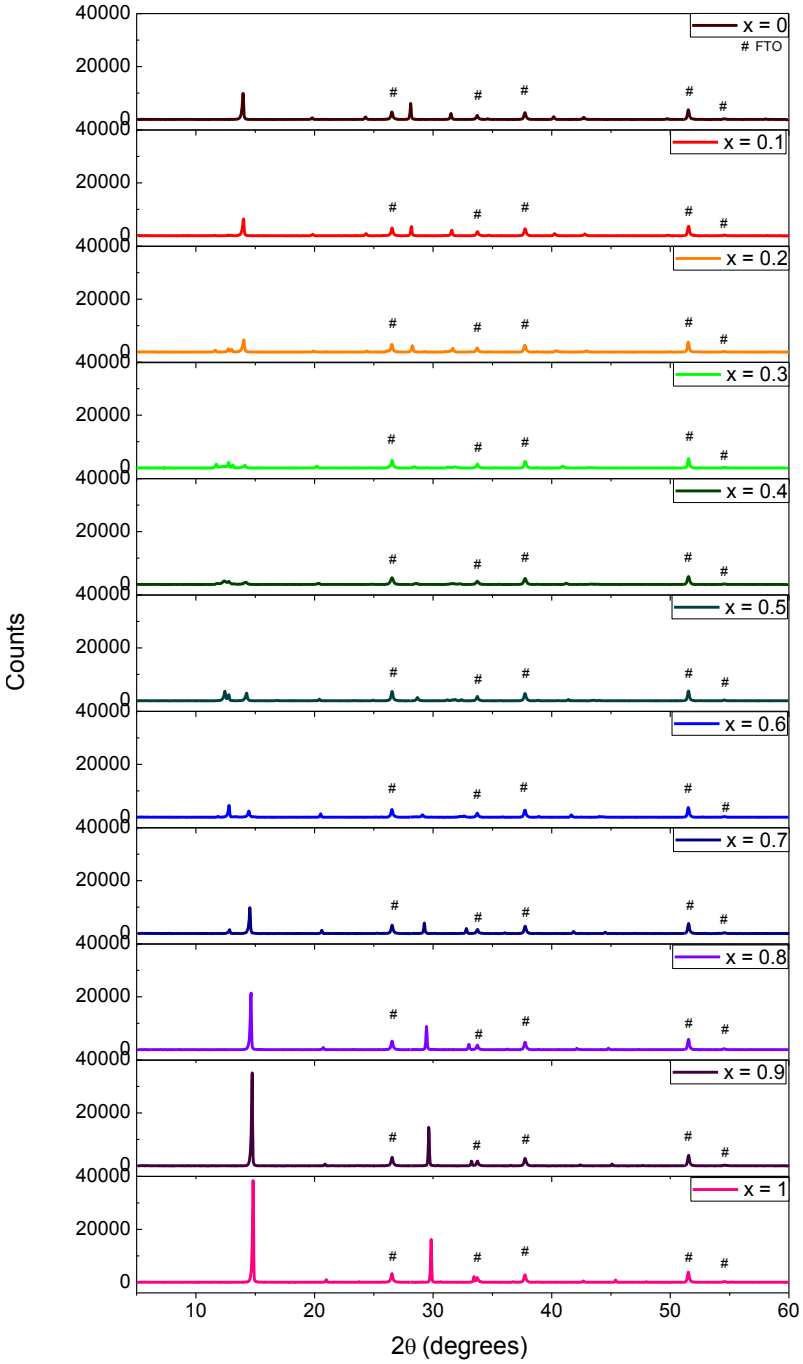

Fig. S1 X-ray diffraction pattern (XRD) for the entire range of $FAPb(I_{(1-x)}Br_{(x)})_3$ perovskites formed on fluorine-doped tin oxide (FTO) coated glass substrates when annealed at 170°C for 10m, using a 0.55M solution. Peaks labelled with # are assigned to the FTO substrate.

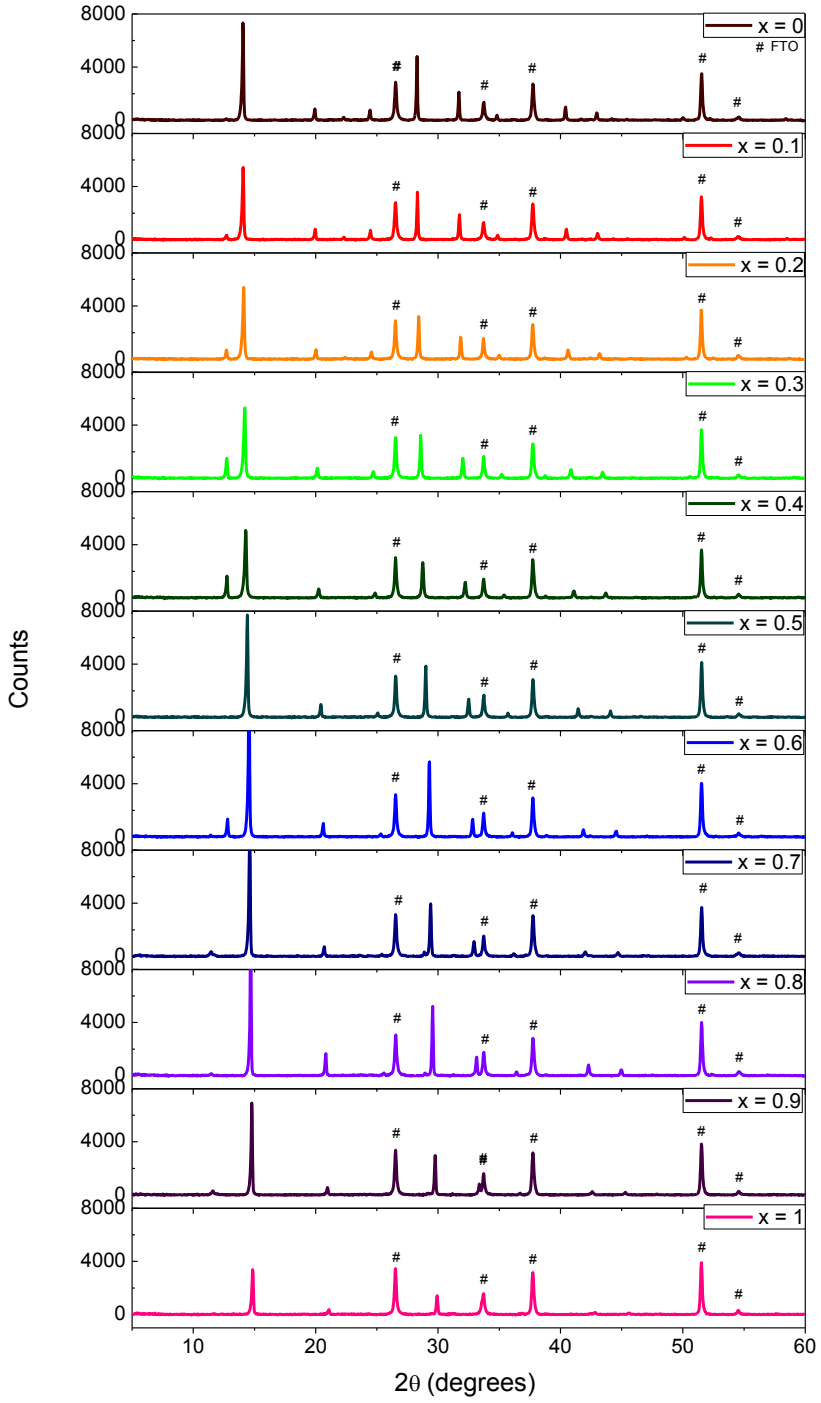

Fig. S2 X-ray diffraction pattern (XRD) for the entire range of $FA_{0.83}Cs_{0.17}Pb(I_{(1-x)}Br_{(x)})_3$ perovskites formed on fluorine-doped tin oxide (FTO) coated glass substrates when annealed at 170°C for 10m. This series were fabricated using a 0.4M, with the exception of x = 0.9 and x = 1, which were fabricated with a 0.2M precursor solution due to poor CsBr solubility in anhydrous N,N-dimethylformamide (DMF).Peaks labelled with # are assigned to the FTO substrate.

Effect of cesium

We have fabricated and characterized a variety of mixed cation lead halide perovskite to investigate the effect of cesium within this perovskite structure. In order to obtain a ~1.75eV optical band gap with a formamidinium lead trihalide perovskite, approximately 40% bromide and 60% iodide mixture is needed (*13*). As we illustrate in Fig. S3, we fabricate thin-films via spin coating using a precursor solution with composition $FA_{(1-x)}Cs_{(x)}Pb(I_{0.6}Br_{0.4})_3$, where x represents the cesium content. We observe that the $FAPb(I_{0.6}Br_{0.4})_3$ composition appears yellowish and has an indistinct absorption edge. As we show in Fig. S3A, a darkening of the film is observed as we substitute formamidinium with cesium. This increase in absorption is confirmed in the absorbance measurements shown in Fig. S3B. Estimation of the band gap from Tauc plots is illustrated in Fig. S4. As we increase the Cs content, we notice a formation of a sharp absorption onset, indicative of a more ordered crystalline perovskite material. Furthermore, as we increase the Cs to FA ratio, we notice an increase in optical band gap towards a higher energy level. Fig. S3B shows the relation between Cs incorporation and optical band gap, where we observe a shift in optical band gap from 1.7 eV to 1.8 eV for x = 0.05 to 0.5. Fig. S3C shows the steady-state PL spectra for Cs content varying from x = 0.1 to 0.5. This range is ideal for fine-tuning of the optical band gap of the top-cell to obtain perfect current matching with a c-Si bottom junction; the changes observed are less extreme than the effect of halide substitution.

Cesium has a smaller ionic radius compared to formamidinium, thus, we expect the lattice to contract as we introduce Cs into the lattice (*41*). A lattice contraction, accompanied by an increase in the octahedral tilting angles (*42*), should result in an increase in optical band gap, which in turn, causes a blue shift in the absorption onset (*12*, *13*). Fig. S3D shows the X-ray diffraction pattern of a range of $FA_{(1-x)}Cs_{(x)}Pb(I_{0.6}Br_{0.4})_3$ (shown in full in Fig. S5). We observe that as more Cs the (100) reflection intensity gradually increases as we add cesium to the formamidinium lead mixed halide perovskite structure. We also observe a contraction of the lattice upon increasing the cesium fraction. This contraction appears to favour the formation of a single crystalline cubic structure. As shown in Fig. S3E, the lattice contraction is consistent with the optical band gap increase for compositions ranging from x = 0.1 to 0.5 Cs. Although we could fabricate films with Cs composition of up to x = 0.75, these films where highly unstable in air and quickly reverted back to a yellow phase within a matter of hours.

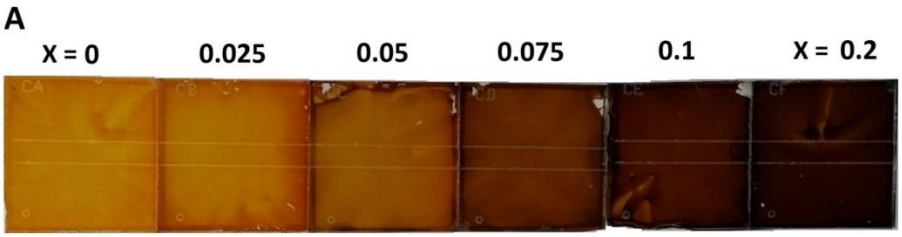

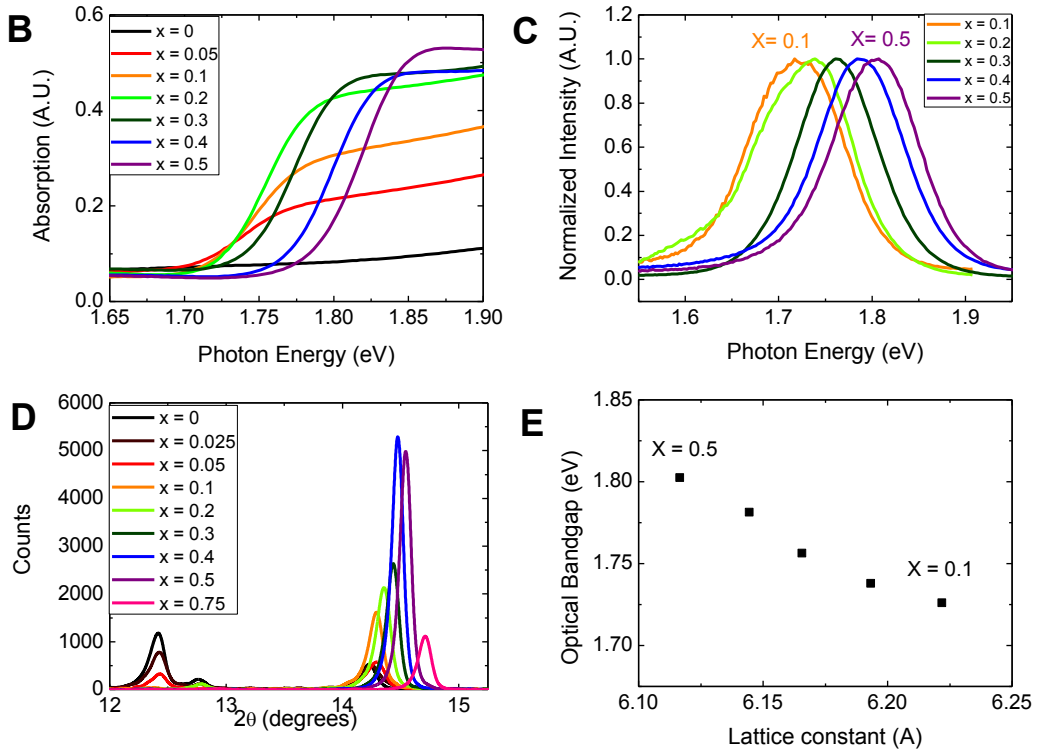

Fig. S3Tunability of the $FA_{(1-x)}Cs_{(x)}Pb(I_{0.6}Br_{0.4})_3$ perovskite system when annealed at 170°C using a 0.55M precursor solution. (**A**) Photograph of perovskite films with Cs composition increasing from x = 0 to 0.2. (**B**) UV-Vis absorbance of perovskite films, where x is varied from 0 to 0.5. (**C**) Steady-state photoluminescence spectra for Cs content varying from X = 0.1 to 0.5. (**D**) X-ray diffraction (XRD) pattern of perovskite material showing the formation of a single crystalline (100) cubic peak and its shift with increasing Cs content from x = 0 to 0.75. (**E**) Optical band gap with cubic lattice parameter as determined from XRD pattern and Tauc plot.

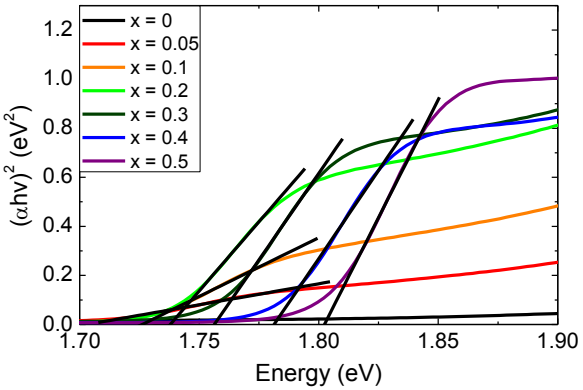

Fig. S4 Tauc plot of $FA_{(1-x)}Cs_xPb(I_{0.6}Br_{0.4})_3$ assuming direct band gap and showing determination of optical band gap from intercept.

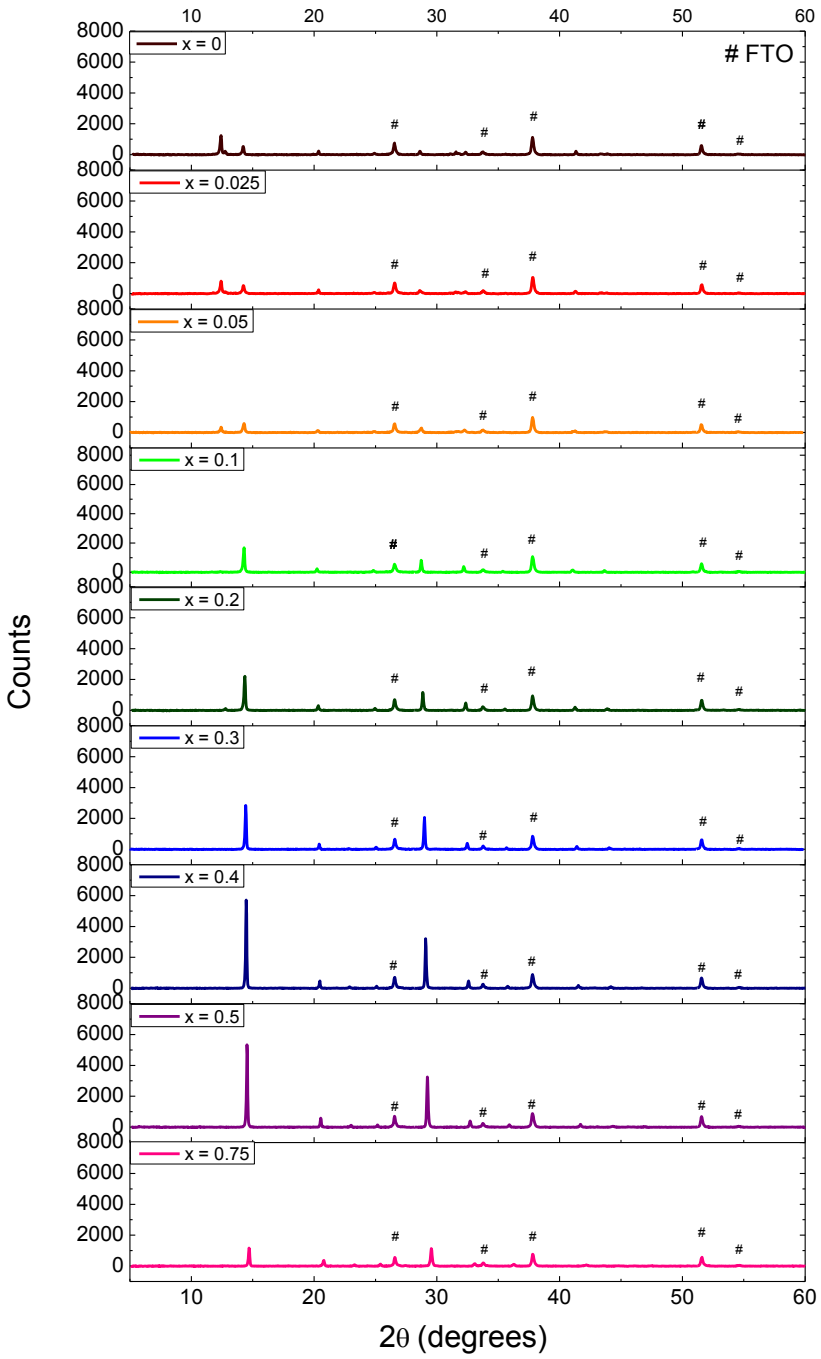

Fig. S5 X-ray diffraction pattern (XRD) for the full range of $FA_{(1-x)}Cs_{(x)}Pb(I_{0.6}Br_{0.4})_3$ perovskites formed on fluorine-doped tin oxide (FTO) coated glass substrates when annealed at 170°C for 10m, using a 0.55M solution. Peaks labelled with # are assigned to the FTO substrate.

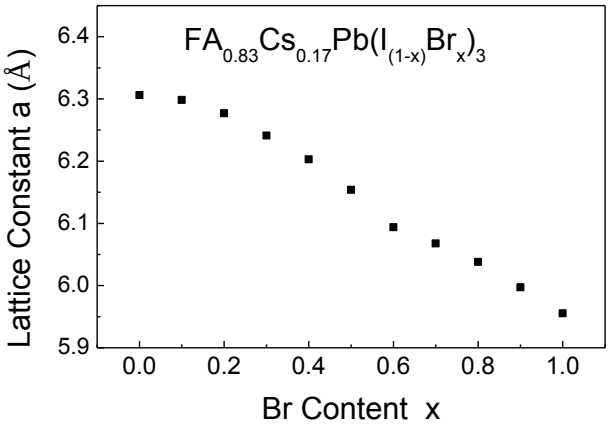

Fig. S6 Lattice Constant of $FA_{0.83}Cs_{0.17}Pb(I_{(1-x)}Br_{(x)})_3$ perovskite system plotted as a function of bromide content. This linear relationship between lattice constant and bromide content indicates that this system follows Vegard's law.

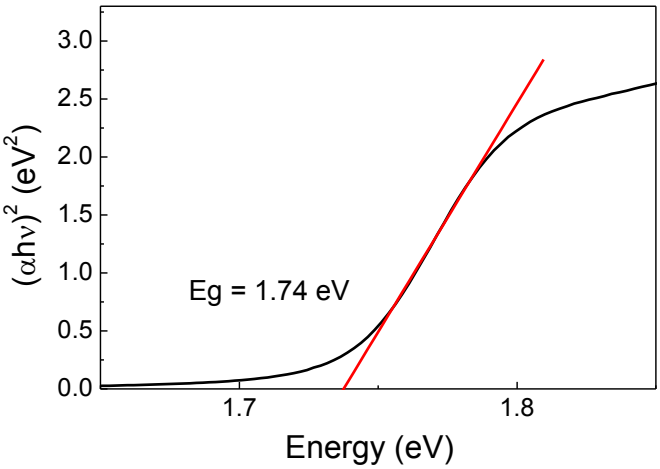

Fig. S7 Tauc plot of $FA_{0.83}Cs_{0.17}Pb(I_{0.6}Br_{0.4})_3$ assuming direct band gap and showing determination of optical band gap from intercept.

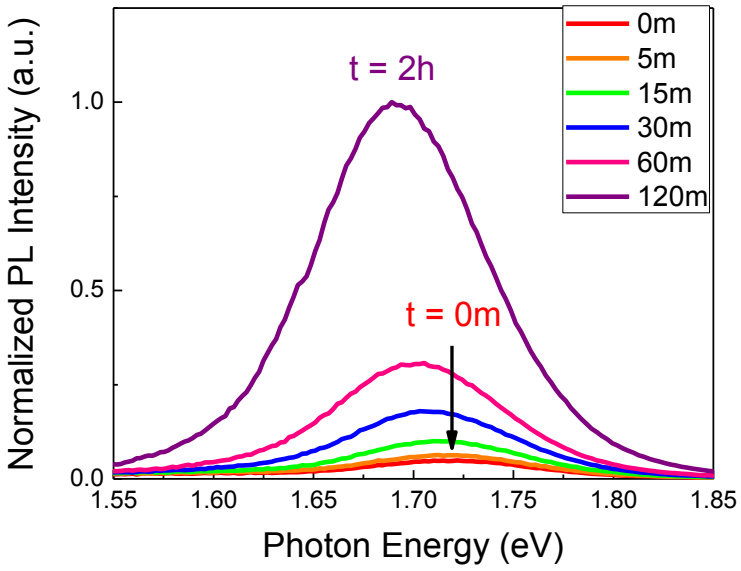

Fig. S8. Normalized photoluminescence (PL) measurement of the $MAPb(I_{0.8}Br_{0.2})_3$ thin film, measured after 0, 5, 15, 30 and 60 minutes of light exposure using a power density of ~3 mW cm^{-2} and a wavelength of 550nnm as excitation source.

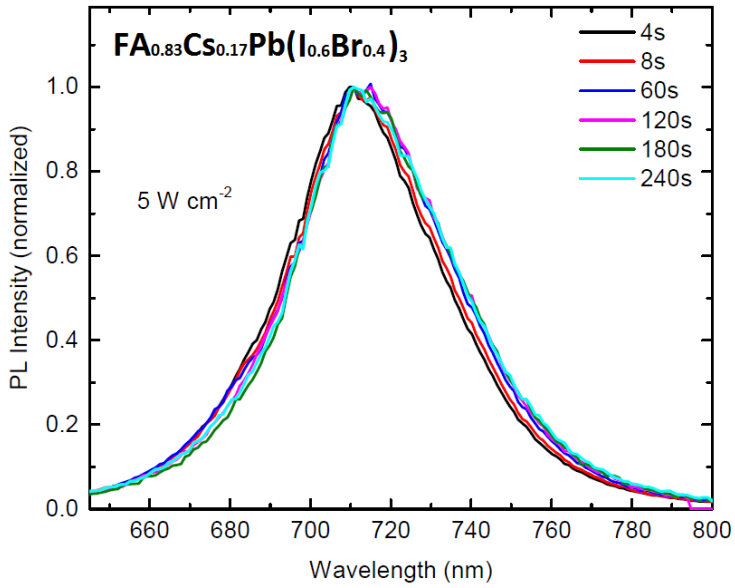

Fig. S9 Photoluminescence spectra of $FA_{0.83}Cs_{0.17}Pb(I_{0.6}Br_{0.4})_3$ following excitation with pulse fluence of 0.5 µJcm^{-2} and laser intensity of 5 Wcm^{-2} at a wavelength of 405 nm.

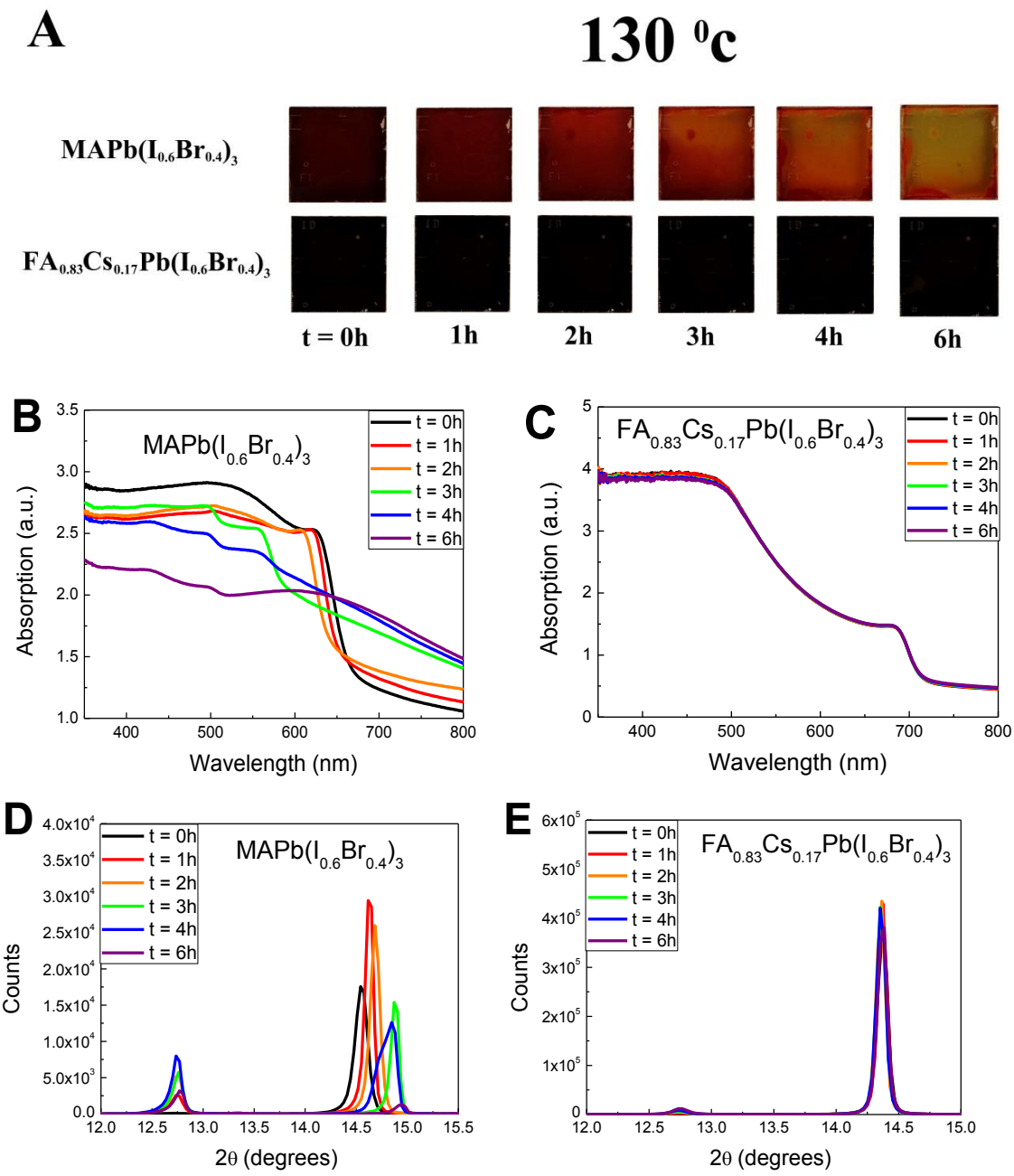

Fig S10. Mixed-halide perovskite films heated on a 130c hotplate inside a N_2 glovebox (~4ppm O_2 and ~0.5ppm H_2O) for a period of up to 6 hours. (**A**) Images (**B**) UV-VIS absorption of $MAPb(I_{0.4}Br_{0.6})_3$ (**C**) UV-VIS absorption of $FA_{0.83}Cs_{0.17}Pb(I_{0.4}Br_{0.6})_3$ (**D**) XRD of $MAPb(I_{0.4}Br_{0.6})_3$ (**E**) XRD of $FA_{0.83}Cs_{0.17}Pb(I_{0.4}Br_{0.6})_3$

Device Optimization

We fabricated a series of $FA_{(1-x)}Cs_{(x)}Pb(I_{0.6}Br_{0.4})_3$ planar heterojunction perovskite solar cells with a cesium content ranging from x = 0 to 0.5. Although the crystallinity

appears to increase up to compositions containing x = 0.4 of Cs, device efficiency did not follow. As illustrated in Fig. S11A, we observed a significant increase in maximum power conversion (PCE) with x = 0.1 of Cs, compared to x = 0 Cs content. However, we observed a reduction in PCE as we approach the x = 0.5 Cs content. This loss in efficiency is induced by a drop in fill factor (FF), which appears to be associated with a rise in series resistance (shown in Fig. S11B). We obtained the highest PCEs for a cesium fraction of x = 0.17. As a result, we fixed the cation and halide precursor solution mixture to obtain a precursor composition of $FA_{0.83}Cs_{0.17}Pb(I_{0.6}Br_{0.4})_3$.

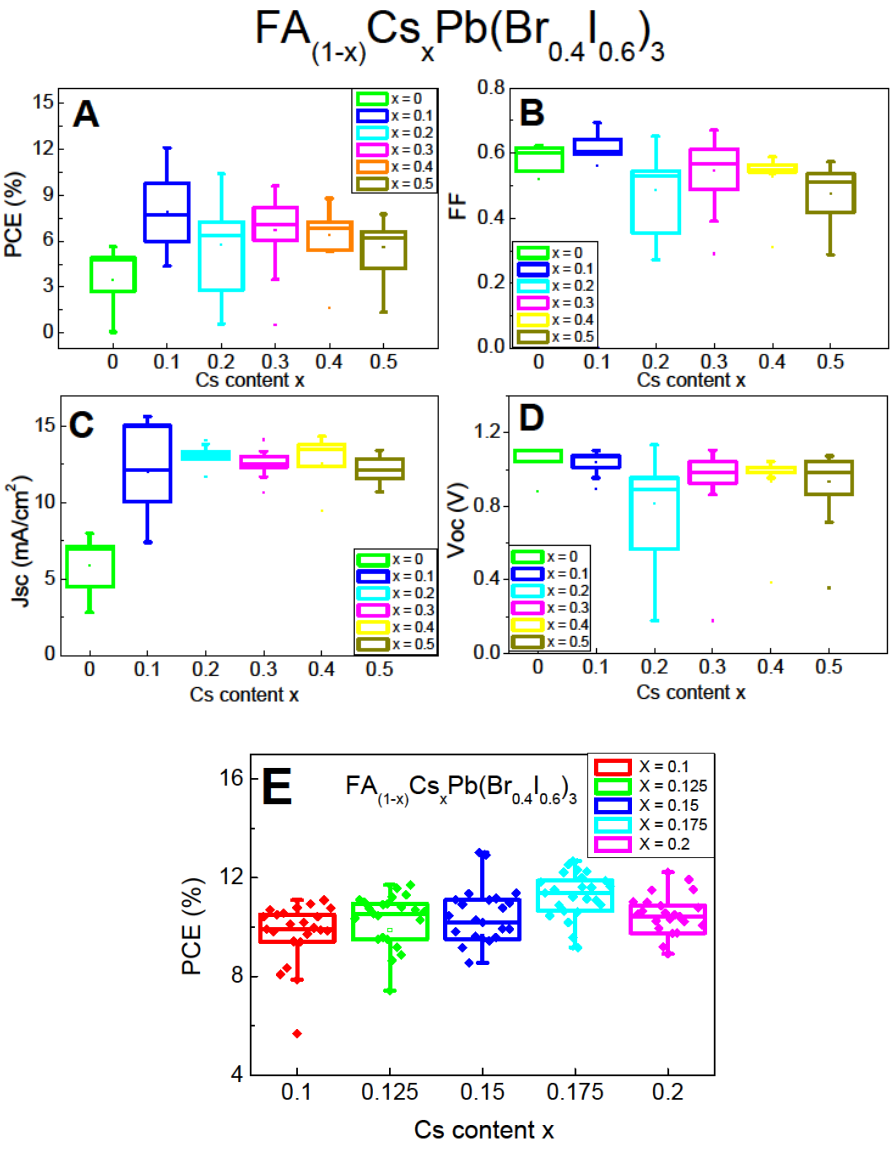

Fig. S11 Device performance of a series of $FA_{(1-x)}Cs_{(x)}Pb(I_{0.6}Br_{0.4})_3$ with various FA/Cs compositions. (**A**) Power conversion efficiency (PCE) of composition ranging from x = 0 to 0.5 of Cs (**B**) Fill factor (FF) (**C**) Short-circuit current density (J_{SC}) (**D**) Open-circuit voltage (V_{OC}) (**E**) PCE of composition ranging from x = 0.1 to 0.2 of Cs content.

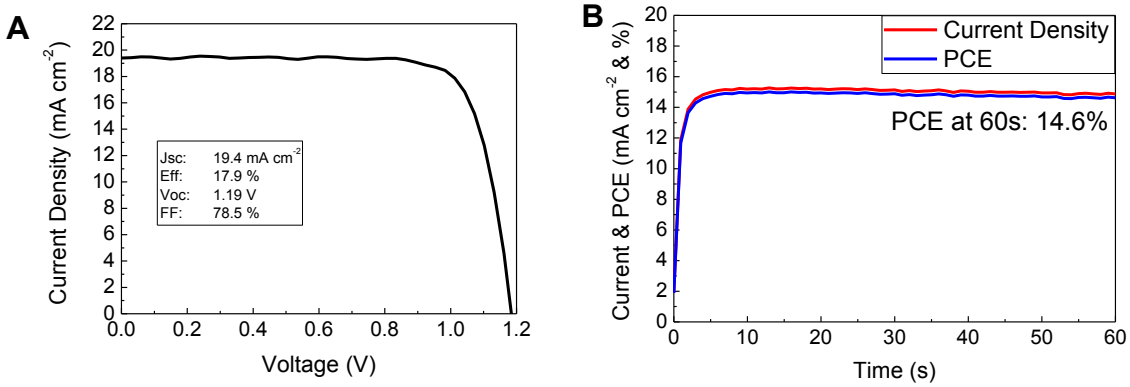

Fig. S12. Current–voltage characteristics of devices under simulated air-mass (AM) 1.5 100 mW cm^{-2} sun light using a 0.38V/s scan rate and photocurrent density and power conversion efficiency as a function of time held at maximum power voltage obtained for the optimized precursor solution composition of $FA_{0.83}Cs_{0.17}Pb(I_{0.6}Br_{0.4})_3$. (**A**) J-V characteristics of FTO/SnO_2/PCBM/perovskite/Spiro-OMeTAD/Ag architecture. (**B**) Photocurrent density and power conversion efficiency measured over 1 minute.

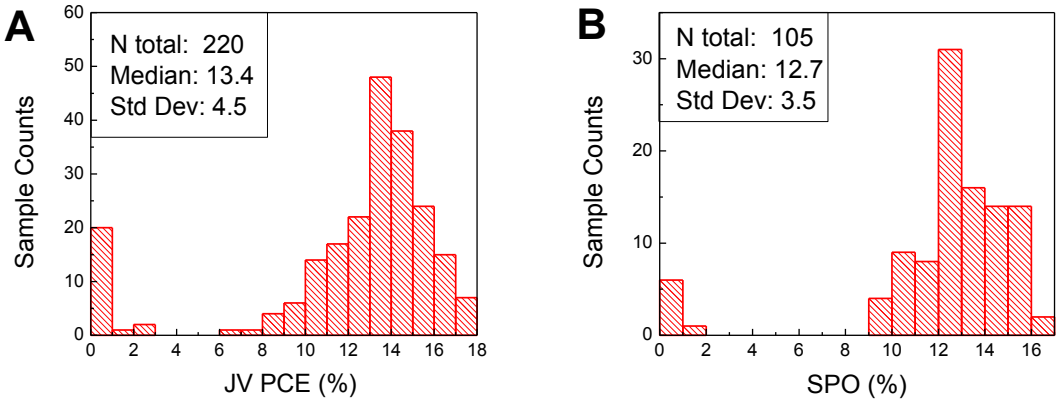

Fig. S13. Histogram of solar cell efficiency of $FA_{0.83}Cs_{0.17}Pb(I_{0.4}Br_{0.6})_3$ perovskite composition. (**A**) JV Power conversion efficiency (PCE) (**B**) Stabilized power output (SPO)

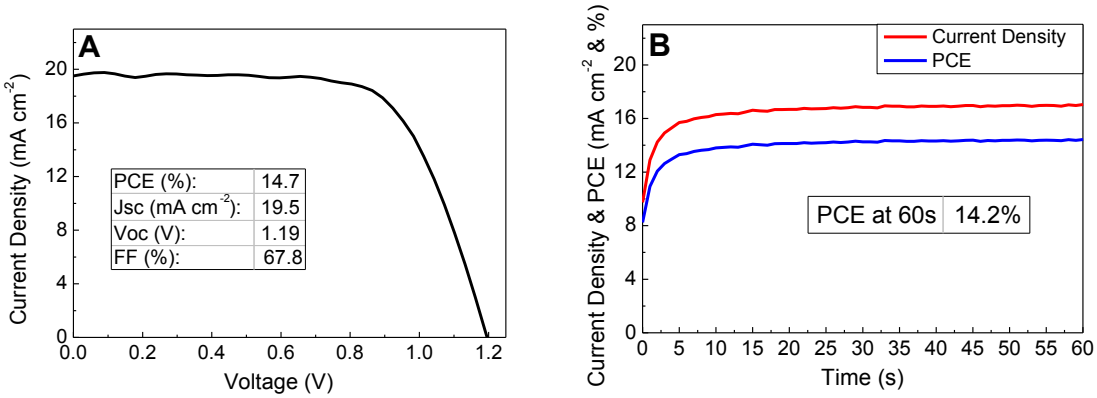

Fig. S14. **Current–voltage characteristics of devices, measured using an active area and masked aperture of 0.715 cm^2, under simulated air-mass (AM) 1.5, 109 mW cm^{-2} sun light using a 0.38V/s scan rate and photocurrent density and power conversion efficiency as a function of time held at maximum power voltage obtained for the optimized precursor solution composition of $FA_{0.83}Cs_{0.17}Pb(I_{0.6}Br_{0.4})_3$.** (**A**) J-V characteristics of FTO/SnO_2/PCBM/perovskite/Spiro-OMeTAD/Ag architecture. (**B**) Photocurrent density and power conversion efficiency measured over 1 minute.

Calculation of the achievable V_{OC}

We calculated the achievable V_{OC} in the radiative limit with the optoelectronic reciprocity relation theory introduced by Rau et al.(36). The short-circuit photocurrent (J_{SC}) is derived by integrating the photovoltaic external quantum efficiency (EQE_{PV}) multiplied with the photon flux of the solar spectrum ($\Phi_{AM1.5}$) over all photon energies as:

$$J_{SC} = q \int EQE_{PV}(E)\Phi_{AM1.5}(E)dE$$

Furthermore, in the dark, all absorbed photons from the environment (assumed photon flux from a black body at 300K Φ_{BB}) are reemitted due to energy conservation. Fig. S15 shows the calculated photon flux of a black body at 300K compared to the photon flux from the solar spectrum at AM1.5. Following Shockley's diode law, under a given bias voltage the probability of the reemission can be described by Fermi-Dirac statistics and approximated with a Boltzmann term. The dark saturation current can then be described by the electroluminescence external quantum efficiency (EQE_{EL}) and the EQE_{PV} of the device:

$$J_0(V) = \frac{q}{EQE_{EL}} \int EQE_{PV}(E)\Phi_{BB}(E)dE \left(e^{\frac{qV}{k_BT}} - 1\right)$$

Combining both currents leads to the current-voltage relationship $J(V) = J_{SC} - J_0(V)$. If we set J = 0 and solve the equation for voltage, we end up with the V_{OC}:

$$V_{OC} = \frac{k_BT}{q} \ln\left(\frac{J_{SC}}{J_0} + 1\right)$$

In the radiative limit, we assume zero non-radiative recombination and can therefore set $EQE_{EL} = 1$, to get the V_{OC} in the radiative limit:

$$V_{OC,rad} = \frac{k_BT}{q} \ln\left(\frac{\int EQE_{PV}(E)\Phi_{AM1.5}(E)dE}{\int EQE_{PV}(E)\Phi_{BB}(E)dE} + 1\right)$$

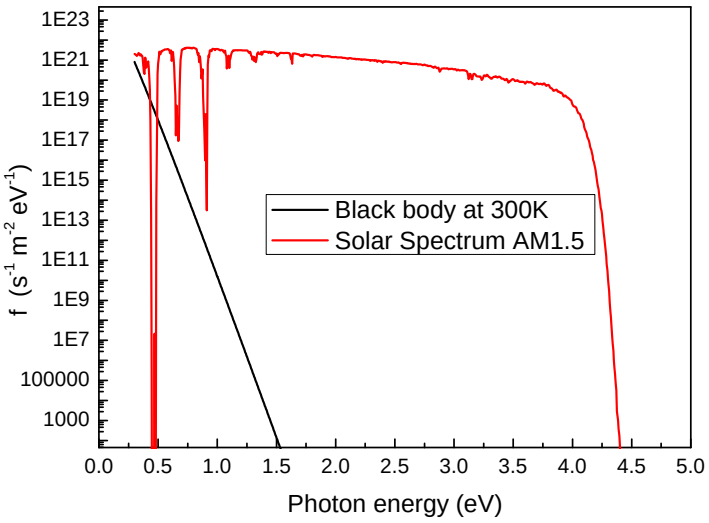

Fig. S15 Calculated photon flux of black body at 300K compared to AM1.5 solar spectrum photon flux.

.

.

.

.

.

REFERENCES AND NOTES

1. V. Sivaram, S. D. Stranks, H. J. Snaith, Out shining silicon. *Sci. Am.* **313**, 54–59 (2015). Medline doi:10.1038/scientificamerican0715-54

2. M. A. Green, K. Emery, Y. Hishikawa, W. Warta, E. D. Dunlop, Solar cell efficiency tables (version 46). *Prog. Photovolt. Res. Appl.* **23**, 805–812 (2015). doi:10.1002/pip.2637

3. A. Shah, P. Torres, R. Tscharner, N. Wyrsch, H. Keppner, Photovoltaic technology: The case for thin-film solar cells. *Science* **285**, 692–698 (1999). Medline doi:10.1126/science.285.5428.692

4. C. R. Kagan, D. B. Mitzi, C. D. Dimitrakopoulos, Organic-inorganic hybrid materials as semiconducting channels in thin-film field-effect transistors. *Science* **286**, 945–947 (1999). Medline doi:10.1126/science.286.5441.945

5. A. Kojima, K. Teshima, Y. Shirai, T. Miyasaka, Organo metal halide perovskites as visible-light sensitizer for photovoltaic cells. *Priv. Commun.* **1**, 1 (2009).

6. M. M. Lee, J. Teuscher, T. Miyasaka, T. N. Murakami, H. J. Snaith, Efficient hybrid solar cells based on meso-superstructured organometal halide perovskites. *Science* **338**, 643–647 (2012). Medline doi:10.1126/science.1228604

7. M. Liu, M. B. Johnston, H. J. Snaith, Efficient planar heterojunction perovskite solar cells by vapour deposition. *Nature* **501**, 395–398 (2013). Medline doi:10.1038/nature12509

8. J. Burschka, N. Pellet, S. J. Moon, R. Humphry-Baker, P. Gao, M. K. Nazeeruddin, M. Grätzel, Sequential deposition as a route to high-performance perovskite-sensitized solar cells. *Nature* **499**, 316–319 (2013). Medline doi:10.1038/nature12340

9. M. Green, A. Ho-Baillie, H. J. Snaith, The emergence of perovskite solar cells. *Nat. Photonics* **8**, 506–514 (2014). doi:10.1038/nphoton.2014.134

10. N. J. Jeon, J. H. Noh, Y. C. Kim, W. S. Yang, S. Ryu, S. I. Seok, Solvent engineering for high-performance inorganic-organic hybrid perovskite solar cells. *Nat. Mater.* **13**, 897–903 (2014). Medline doi:10.1038/nmat4014

11. N. J. Jeon, J. H. Noh, W. S. Yang, Y. C. Kim, S. Ryu, J. Seo, S. I. Seok, Compositional engineering of perovskite materials for high-performance solar cells. *Nature* **517**, 476–480 (2015). Medline doi:10.1038/nature14133

12. J. H. Noh, S. H. Im, J. H. Heo, T. N. Mandal, S. I. Seok, Chemical management for colorful, efficient, and stable inorganic-organic hybrid nanostructured solar cells. *Nano Lett.* **13**, 1764–1769 (2013). Medline doi:10.1021/nl400349b

13. G. E. Eperon, S. D. Stranks, C. Menelaou, M. B. Johnston, L. M. Herz, H. J. Snaith, Formamidinium lead trihalide: A broadly tunable perovskite for efficient planar heterojunction solar cells. *Energy Environ. Sci.* **7**, 982 (2014). doi:10.1039/c3ee43822h

14. W. S. Yang, J. H. Noh, N. J. Jeon, Y. C. Kim, S. Ryu, J. Seo, S. I. Seok, High-performance photovoltaic perovskite layers fabricated through intramolecular exchange. *Science* **348**, 1234–1237 (2015). Medline

15. E. T. Hoke, D. J. Slotcavage, E. R. Dohner, A. R. Bowring, H. I. Karunadasa, M. D. McGehee, Reversible photo-induced trap formation in mixed-halide hybrid perovskites for photovoltaics. *Chem. Sci.* **6**, 613–617 (2015). doi:10.1039/C4SC03141E

16. B. Conings, J. Drijkoningen, N. Gauquelin, A. Babayigit, J. D'Haen, L. D'Olieslaeger, A. Ethirajan, J. Verbeeck, J. Manca, E. Mosconi, F. De Angelis, H. Boyen, Intrinsic thermal instability of methylammonium lead trihalide perovskite. *Adv. Energy Mater.* 10.1002/aenm.201500477 (2015).

17. W. Rehman *et al*., Charge-carrier dynamics and mobilities in formamidinium lead mixed-halide perovskites. *Adv. Mater.* **27**, 7938–7944 (2015).

18. C. D. Bailie, M. G. Christoforo, J. P. Mailoa, A. R. Bowring, E. L. Unger, W. H. Nguyen, J. Burschka, N. Pellet, J. Z. Lee, M. Grätzel, R. Noufi, T. Buonassisi, A. Salleo, M. D. McGehee, Semi-transparent perovskite solar cells for tandems with silicon and CIGS. *Energy Environ. Sci.* **8**, 956–963 (2015). doi:10.1039/C4EE03322A

19. P. Löper, S. J. Moon, S. M. de Nicolas, B. Niesen, M. Ledinsky, S. Nicolay, J. Bailat, J. H. Yum, S. De Wolf, C. Ballif, Organic-inorganic halide perovskite/crystalline silicon four-terminal tandem solar cells. *Phys. Chem. Chem. Phys.* **17**, 1619–1629 (2015). Medline doi:10.1039/C4CP03788J

20. S. Albrecht, M. Saliba, J. Correa Baena, F. Lang, L. Kegelmann, M. Mews, L. Steier, A. Abate, J. Rappich, L. Korte, R. Schlatmann, M. K. Nazeeruddin, A. Hagfeldt, M. Grätzel, B. Rech, Monolithic perovskite/silicon-heterojunction tandem solar cellsprocessed at low temperature. *Energy Environ. Sci.* 10.1039/C5EE02965A (2015).

21. A. Binek, F. C. Hanusch, P. Docampo, T. Bein, Stabilization of the trigonal high-temperature phase of formamidinium lead iodide. *J. Phys. Chem. Lett.* **6**, 1249–1253 (2015). Medline doi:10.1021/acs.jpclett.5b00380

22. S. Pang, H. Hu, J. Zhang, S. Lv, Y. Yu, F. Wei, T. Qin, H. Xu, Z. Liu, G. Cui, $NH_2CH{=}NH_2PbI_3$: An alternative organolead iodide perovskite sensitizer for mesoscopic solar cells. *Chem. Mater.* **26**, 1485–1491 (2014). doi:10.1021/cm404006p

23. C. C. Stoumpos, C. D. Malliakas, M. G. Kanatzidis, Semiconducting tin and lead iodide perovskites with organic cations: Phase transitions, high mobilities, and near-infrared photoluminescent properties. *Inorg. Chem.* **52**, 9019–9038 (2013). Medline doi:10.1021/ic401215x

24. N. Pellet, P. Gao, G. Gregori, T. Y. Yang, M. K. Nazeeruddin, J. Maier, M. Grätzel, Mixed-organic-cation perovskite photovoltaics for enhanced solar-light harvesting. *Angew. Chem. Int. Ed. Engl.* **53**, 3151–3157 (2014). Medline doi:10.1002/anie.201309361

25. S. D. Stranks, H. J. Snaith, Metal-halide perovskites for photovoltaic and light-emitting devices. *Nat. Nanotechnol.* **10**, 391–402 (2015). Medline doi:10.1038/nnano.2015.90

26. J.-W. Lee, D.-H. Kim, H.-S. Kim, S.-W. Seo, S. M. Cho, N.-G. Park, Formamidinium and cesium hybridization for photo- and moisture-stable perovskite solar cell. *Adv. Energy Mater.* 10.1002/aenm.201501310 (2015).

27. H. Choi, J. Jeong, H.-B. Kim, S. Kim, B. Walker, G.-H. Kim, J. Y. Kim, Cesium-doped methylammonium lead iodide perovskite light absorber for hybrid solar cells. *Nano Energy* **7**, 80–85 (2014). doi:10.1016/j.nanoen.2014.04.017

28. See the supplementary materials on *Science* Online.

29. C. Bi, Y. Yuan, Y. Fang, J. Huang, Low-temperature fabrication of efficient wide-bandgap organolead trihalide perovskite solar cells. *Adv. Energy Mater.* 10.1002/aenm.201401616 (2014).

30. K. Tvingstedt, O. Malinkiewicz, A. Baumann, C. Deibel, H. J. Snaith, V. Dyakonov, H. J. Bolink, Radiative efficiency of lead iodide based perovskite solar cells. *Sci. Rep.* **4**, 6071 (2014). Medline doi:10.1038/srep06071

31. S. De Wolf, J. Holovsky, S. J. Moon, P. Löper, B. Niesen, M. Ledinsky, F. J. Haug, J. H. Yum, C. Ballif, Organometallic halide perovskites: Sharp optical absorption edge and its relation to photovoltaic performance. *J. Phys. Chem. Lett.* **5**, 1035–1039 (2014). Medline doi:10.1021/jz500279b

32. A. Sadhanala, F. Deschler, T. H. Thomas, S. E. Dutton, K. C. Goedel, F. C. Hanusch, M. L. Lai, U. Steiner, T. Bein, P. Docampo, D. Cahen, R. H. Friend, Preparation of single-phase films of $CH_3NH_3Pb(I_{1-x}Br_x)_3$ with sharp optical band edges. *J. Phys. Chem. Lett.* **5**, 2501–2505 (2014). Medline doi:10.1021/jz501332v

33. R. L. Milot, G. E. Eperon, H. J. Snaith, M. B. Johnston, L. M. Herz, Temperature-dependent charge-carrier dynamics in $CH_3NH_3PbI_3$ perovskite thin films. *Adv. Funct. Mater.* **25**, 6218–6227 (2015).

34. W. Tress *et al*., Predicting the open-circuit voltage of $CH_3NH_3PbI_3$ perovskite solar cells using electroluminescence and photovoltaic quantum efficiency spectra: the role of radiative and non-radiative recombination. *Adv. Energy Mater.* 10.1002/aenm.201400812 (2014).

35. H. J. Snaith, Estimating the maximum attainable efficiency in dye-sensitized solar cells. *Adv. Funct. Mater.* **20**, 13–19 (2010). doi:10.1002/adfm.200901476

36. U. Rau, Reciprocity relation between photovoltaic quantum efficiency and electroluminescent emission of solar cells. *Phys. Rev. B* **76**, 085303 (2007). doi:10.1103/PhysRevB.76.085303

37. L. Mazzarella, S. Kirner, B. Stannowski, L. Korte, B. Rech, R. Schlatmann, p-type microcrystalline silicon oxide emitter for silicon heterojunction solar cells allowing current densities above 40 mA/cm^2. *Appl. Phys. Lett.* **106**, 023902 (2015). doi:10.1063/1.4905906

38. S.-M. Yong, N. Tsvetkov, L. Larina, B. T. Ahn, D. K. Kim, Ultrathin SnO_2 layer for efficient carrier collection in dye-sensitized solar cells. *Thin Solid Films* **556**, 503–508 (2014). doi:10.1016/j.tsf.2014.01.008

39. K. Wojciechowski, T. Leijtens, S. Siprova, C. Schlueter, M. T. Hörantner, J. T. Wang, C. Z. Li, A. K. Jen, T. L. Lee, H. J. Snaith, C60 as an efficient n-type compact layer in perovskite solar cells. *J. Phys. Chem. Lett.* **6**, 2399–2405 (2015). Medline

40. K. Wojciechowski, S. D. Stranks, A. Abate, G. Sadoughi, A. Sadhanala, N. Kopidakis, G. Rumbles, C. Z. Li, R. H. Friend, A. K. Jen, H. J. Snaith, Heterojunction modification for highly efficient organic-inorganic perovskite solar cells. *ACS Nano* **8**, 12701–12709 (2014). Medline doi:10.1021/nn505723h

41. I. Borriello, G. Cantele, D. Ninno, Ab initio investigation of hybrid organic-inorganic perovskites based on tin halides. *Phys. Rev. B* **77**, 235214 (2008). doi:10.1103/PhysRevB.77.235214

42. M. R. Filip, G. E. Eperon, H. J. Snaith, F. Giustino, Steric engineering of metal-halide perovskites with tunable optical band gaps. *Nat. Commun.* **5**, 5757 (2014). Medline doi:10.1038/ncomms6757